Chapter 9
Modeling of Whole-Heart Electrophysiology and Mechanics: Toward Patient-Specific Simulations

Fijoy Vadakkumpadan, Viatcheslav Gurev, Jason Constantino, Hermenegild Arevalo, and Natalia Trayanova

9.1 Introduction

The practice of cardiovascular care has seen significant advances in the past 40 years with dramatic reduction of mortality from heart diseases. Nevertheless, cardiac diseases remain the leading cause of morbidity and mortality in the developed world and are on the rise in developing countries [37]. It is well recognized that the conventional clinical practice of using population-based metrics to prescribe "one size fits all" treatment methods does not provide optimal health care for many patients because of the individual variability in pathophysiology. Moreover, in many situations, physicians do not have a way of predicting patient responses to various therapeutic interventions, and therefore have to rely on "trial and error" to identify the treatment-response relationship. An emerging paradigm that addresses these challenges is the so-called personalized medicine, which seeks to develop diagnosis and treatment methods that can be tailored by the physician a priori according to the specific needs of an individual patient [25, 44, 52]. Application of such personalized approach to cardiac care can dramatically improve the treatment of heart diseases. To fully utilize the quality and diversity of clinically available data for personalized cardiac care, it is necessary to integrate structural and functional data at molecular, cellular, tissue, and organ level into a consistent framework which can be used to predict the outcomes of therapeutic interventions. Computational modeling provides a powerful tool to perform this data integration [29, 32].

Among the different data collection techniques, imaging has attained special significance due to the recent advances in acquisition technologies. Ex vivo magnetic resonance imaging (MRI) technologies have facilitated the acquisition of geometry and tissue architecture of the heart at very high spatial resolution. Modern ex vivo anatomical MR scanners can image the cardiac histoanatomy of small experimental animals, such as rabbit, with an isotropic resolution in the order of 10^{-5} m [11].

F. Vadakkumpadan (✉)
Institute for Computational Medicine and Department of Biomedical Engineering,
Johns Hopkins University, CSEB Room 218, 3400 N Charles St, Baltimore, MD 21218, USA
e-mail: fijoy@jhu.edu

R.C.P. Kerckhoffs (ed.), *Patient-Specific Modeling of the Cardiovascular System: Technology-Driven Personalized Medicine*, DOI 10.1007/978-1-4419-6691-9_9,

Advanced ex vivo diffusion tensor (DT) MR equipments can measure the diffusivity of water in the tissue with a resolution in the order of 10^{-4} m [20]. The primary eigenvectors of the DTs have been shown to be aligned with the fiber orientations. Evidence also suggests that the secondary and tertiary eigenvectors are oriented normally to the main cell axes, in the myocardial laminar plane and perpendicular to it, respectively. These developments in ex vivo imaging have facilitated the construction of image-based representative models of cardiac structure with unprecedented detail [32, 49]. Similarly, advances in in vivo imaging methods have placed at physicians' disposal the structural details of patient hearts in hitherto unavailable detail. State-of-the-art MRI and computed tomography (CT) methods can image the myocardial geometry of patient hearts at resolutions that are less than a millimeter [15, 30]. Furthermore, it is now feasible to use MRI in combination with late gadolinium enhancement to acquire the geometry of scar and peri-infarct zones of patient hearts with myocardial infarction [39]. These advances have placed image-based modeling at the threshold of patient-specific applications.

The purpose of this chapter is twofold. First, we briefly explain the methods we have developed to construct high-resolution representative models of the whole-heart electrophysiology and electromechanics from images acquired ex vivo. Second, we present a pipeline that we have implemented to estimate patient-specific myocardial fiber orientations from in vivo images. The whole-heart electrophysiology is modeled using a continuum approximation of tissue properties, which accounts for current fluxes in the extracellular and intracellular spaces, transmembrane currents through ionic channels, pumps, and exchangers, as well as changes in ionic concentrations including intracellular calcium cycling. The electromechanical modeling incorporates, in addition to cardiac electrophysiology, representations of the myofilament dynamics, ventricular contraction, and blood flow through the circulatory system. These modeling techniques in combination with the proposed methodology for estimating patient-specific cardiac fiber orientations constitute a step toward personalized simulations of cardiac electrophysiology and mechanics.

In the following, Sect. 9.2 describes our methods for segmenting high-resolution ex vivo images of the heart, Sect. 9.3 describes our methods for generating electrophysiological meshes from segmented images, Sect. 9.4 outlines the generation of mechanical meshes, Sect. 9.5 explains our methodology for simulating cardiac electrophysiology, Sect. 9.6 presents our methodology for simulating cardiac electromechanics, Sect. 9.7 outlines the electrophysiological modeling of an infarcted canine heart, Sect. 9.8 presents the electromechanical modeling of a normal canine heart, and Sect. 9.9 presents our pipeline for generating patient-specific computational cardiac meshes. Section 9.10 concludes the chapter.

9.2 Image Segmentation

To generate image-based models of the heart, it is necessary to classify (or segment) the voxels in the structural MR image into different groups, such as normal tissue, diseased tissue (or infarct), background, etc. We developed a processing pipeline

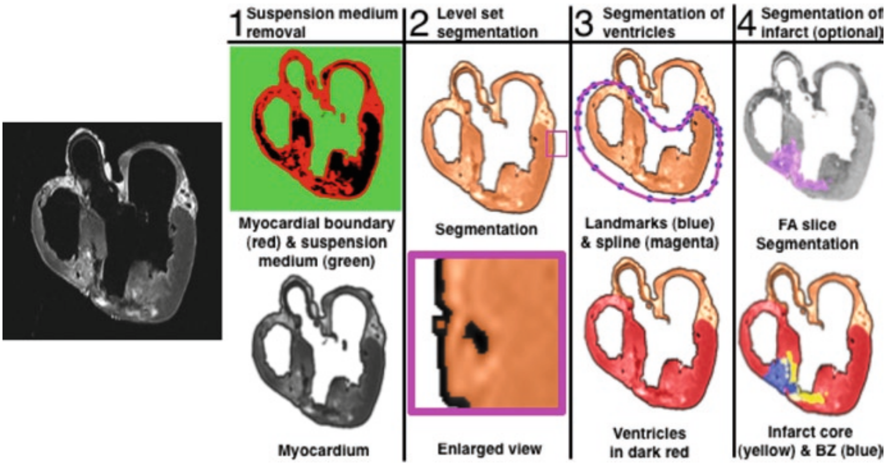

Fig. 9.1 The processing pipeline we have developed to generate computational models of the whole heart from high-resolution ex vivo structural MR images

for the segmentation of the structural MR image as illustrated in Fig. 9.1. The figure shows the results as an example image slice is processed through the steps 1–4 in the pipeline. The original example slice is shown in the leftmost column of the figure. The steps of the pipeline are briefly explained in detail below. More details of our segmentation methodology can be found elsewhere [48, 49].

9.2.1 Suspension Medium Removal

In the first step of our segmentation pipeline, the structural MR image is processed to label and "remove" the voxels corresponding to the cavity content, and the medium in which the heart was suspended during the image acquisition. First, the myocardial boundary of the whole heart is extracted using a combination of two-dimensional (2D) edge detection [24] and three-dimensional (3D) region growing [1]. Next, from the image that represents the myocardial boundary, voxels that correspond to the suspension and cavity medium are extracted using the region-growing algorithm. Finally, the suspension medium is removed from the original structural MR image by assigning the background intensity to all voxels that correspond to the medium. Step 1 in Fig. 9.1 shows the myocardial boundary, suspension medium, and myocardium for the example slice.

9.2.2 Level Set Segmentation

In the next step, a level set method is applied to the image of the myocardium to separate the larger coronary arteries and interlaminar clefts, as well as to refine the myocardial boundary extracted during the previous steps. Level set methods have the inherent capability to implicitly track complex topologies [21]. This characteristic makes them highly suitable for the delineation of the complex coronary artery network and interlaminar clefts. Step 2 in Fig. 9.1 illustrates the level set segmentation for the example slice.

9.2.3 Segmentation of Ventricles

In the third step of our pipeline, segmentation of the ventricular myocardium is performed. In this step, in each slice, the ventricular portion of the tissue is labeled by fitting a closed spline curve through landmark points placed around the ventricles and along the atrioventricular border. All voxels that belong to tissue inside the curve are marked as ventricular. Step 3 in Fig. 9.1 shows the landmarks, spline, and ventricular myocardium for the example slice. The identification of landmark points is performed manually for a number of slices that are evenly distributed in the image. The landmarks for the remaining slices are obtained by linearly interpolating the manually identified points.

9.2.4 Infarct Segmentation

Frequently, hearts have undergone structural remodeling, most notable infarction. After the delineation of the ventricles, any infarct tissue present is labeled. First, a fractional anisotropy (FA) image is generated from the DTMR image by computing the FA of the DT at each voxel [8]. FA quantifies the degree of anisotropy – of diffusion of water in the tissue – in a single number. The infarct region is characterized by lower anisotropy [12]. On the basis of this difference in FA values, the infarct region is separated from the normal myocardium by applying the level set segmentation to the 3D FA image. Step 4 in Fig. 9.1 shows the segmentation of the FA image slice that corresponds to the example slice. Next, the infarct region is subdivided into two areas: a core, which is assumed to contain inexcitable scar tissue, and a peri-infarct zone, which is assumed to contain excitable but pathologically remodeled tissue, by thresholding the structural MR image based on the intensity values of the voxels. The core has high or low intensity, while the peri-infarct zone has medium intensity [39, 53]. Step 4 in Fig. 9.1 illustrates the final segmentation of the example slice. Once any infarct areas present are identified, segmentation of the structural MR image is complete.

9.3 Electrical Mesh Generation

The electrical mesh is a finite element mesh in which each element is assigned a unit vector that indicates the orientation of myocardial fibers inside that element. We generate the finite element mesh directly from segmented images using commercial software known as Tarantula (http://www.meshing.at/Spiderhome/Tarantula.html). For details regarding the mesh generation methodology as well as the examination of mesh quality metrics such as aspect ratio, skewness, maximum angle, and minimum angle, the reader is referred to a recent paper [33]. The paper also contains performance metrics of benchmark electrophysiological simulations and a comparison with other mesh generation techniques. The unique advantage of the software is that it can generate unstructured meshes directly from segmented images. Figure 9.2a shows a mesh generated for the processed slice shown in Fig. 9.1. Figure 9.2b presents a small region of the mesh in detail. As the figure illustrates, the interior tissue volume is meshed at low resolution, while the interface between tissue and non-tissue is refined by a factor of about two.

The generation of the electrical mesh is completed by mapping the fiber orientations onto the finite element mesh by interpolating the primary diffusion vectors on the centroids of the elements. First, a reference vector field is constructed by computing the primary eigenvector of each tensor in the previously interpolated DTMR image. This vector field is in the same coordinate system as the finite element mesh. The fiber orientation assigned to an element in the mesh is the direction of that vector in the reference field nearest to the centroid of the element. It must be noted

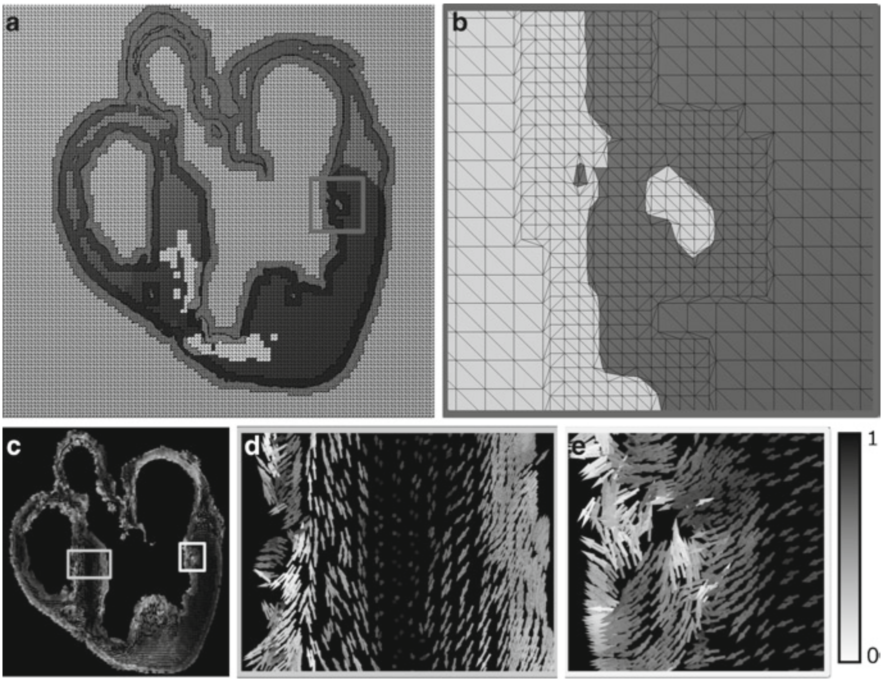

Fig. 9.2 Electrical mesh generation: (**a**) mesh corresponding to the slice shown in Fig 9.1; (**b**) enlarged view of the small region enclosed by the box in (**a**); (**c**) 2D projection, on the *xz* plane, of orientations assigned to the mesh shown in (**a**); (**d**, **e**) show enlarged views of small regions enclosed by the boxes in septum and LV in (**c**), respectively

that the two-step interpolation process correctly handles cases, where two diffusion vectors that form an obtuse angle are close together, because the reference field is constructed based on the interpolation of original diffusion weighted images, and the nearest neighbor interpolation does not involve spatial averaging of multiple vectors. Also, the nearest neighbor interpolation performed here does not produce any artifacts because the spatial resolution of the reference vector field is greater than or equal to that of the mesh in all our data. Figure 9.2c shows the 2D projection, on the *xz* plane, of derived fiber orientations that are mapped to the mesh shown in Fig. 9.2a. The arrows are colored according to the *y* component of the diffusion vectors. Due to the transmural rotation of the fibers [18–20], the arrows are lighter near the epi- and endocardial surfaces, and darker near the midwall. Figure 9.2d shows the enlarged view of a small region in the septum. Since the original slice shown in Fig. 9.1 intersects the septum nearly at a right angle, the rotation of the fibers is evident in Fig. 9.2d: the arrows are longer near the surfaces, where the fibers are oriented in the base–apex direction, and shorter near midwall, where the fibers aligned with the circumferential direction [18–20]. Figure 9.2e shows an enlarged view of a small region in the left ventricular (LV) myocardium. The arrows are densely distributed near the surfaces, demonstrating the higher resolution of the mesh in those regions.

9.4 Mechanical Mesh Generation

In this section, we describe our methods for generating computational meshes for the simulation of cardiac mechanics. The structure of the finite element hexahedral mesh for our mechanical model consists of two 6×6-element layers, as shown in Fig. 9.3a. The portion of the mesh where the two layers are attached formed the LV, the upper detached layer formed the septum, and the remaining lower layer formed

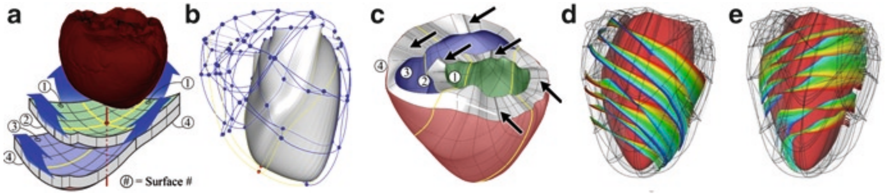

Fig. 9.3 (**a**) Overview of fitting the hexahedral mesh to the geometry obtained from segmenting the MRI scans (*the red mesh*). See text for details. (**b**) Wireframe of the hexahedral mesh. The LV is solid and the RV is transparent. The center node of the *blue surface* (*upper red node*) was positioned to the RV apex. The *yellow lines* correspond to those in panel (**a**). (**c**) Final hexahedral mesh. The *arrows* point to locations where corner elements were removed. Fibers within laminar sheets of normal canine ventricles visualized as streamlines. (**d**, **e**) Visualization of the laminar sheets located near the epicardium and endocardium, respectively. The colors in the sheets trace individual fibers

the right ventricle (RV). Layer surfaces labeled 1–4 in Fig. 9.3a defined the endocardium and epicardium of the ventricles, where surface 1 (green) was the LV endocardium, surfaces 2 and 3 (blue) formed the RV endocardium, and surface 4 (red) defined the epicardium.

To reconstruct the geometry of the mechanical mesh, a least-squares fitting method is used to define the nodal coordinates and their derivatives of the epicardial and endocardial surfaces. This fitting algorithm is described elsewhere [19, 27]. For the nodes that reside within the LV midwall, the spatial coordinates and its derivatives are calculated as the averages of the corresponding nodes on the epicardium and endocardium. To ensure continuity with respect to the global coordinates, all derivatives are defined with respect to arc length, as done by Nielsen et al. [27]. After the fitting, corner elements of the mesh are nearly prisms with two nearly triangular faces, which result in the degeneration of mesh quality. Therefore, the mesh is further refined by decreasing the size of the layers' corner elements and increasing that of the elements adjacent to the corner elements, while retaining the overall shape of the mesh. These smaller corner elements are then removed from the mesh. The arrows in Fig. 9.3c point to the locations of the corner elements. Finally, mesh elements are subdivided to distribute the ventricular volume more evenly among elements. As a result, the initial mesh of 72 elements (Fig. 9.3b) becomes a final hexahedral mesh of 172 elements and 356 nodes (Fig. 9.3c).

The fiber and laminar sheet structural information for the mechanical mesh is obtained from the DTMR image dataset. To this end, tensors and their gradients are defined at each node of the finite element mesh and interpolated within the finite elements using Hermite interpolation. The values at the nodes are computed using a least-squares method, which minimizes the sum of the squared distances between the DTs from the DTMR image and the tensors from the interpolated tensor field. The minimization is performed in the so-called log-Euclidean metric space, which was introduced previously by Arsigny et al. [3]. Since artifacts appear when voxels of MR images represent both ventricular tissue and surrounding media, a regularization of the approximated tensor field was employed to smooth the tensor field and eliminate the partial volume effect on the DTs at the epicardial and endocardial surfaces. The eigenvectors of the tensors in the interpolated tensor field represent the fiber and laminar sheet structure of the reconstructed hearts. Figure 9.3d illustrates the fiber orientations and laminar structure near the epicardium of the anterolateral part of a mechanical mesh that was built using our methods. Figure 9.3e illustrates the fiber orientations and laminar sheets near the endocardium.

9.5 Modeling of Electrophysiology: General Aspects

This section describes the methodology associated with simulating the electrophysiological behavior of the heart. The simulation of propagation of a wave of transmembrane potential is performed by solving a reaction-diffusion partial differential equation (PDE) for the transmembrane potential [31] on the electrical finite element mesh. This equation describes current flow through cardiac cells that are electrically well connected by means of low-resistance gap junctions, allowing for a continuum representation of current flow in the heart. Cardiac tissue has orthotropic passive electrical conductivities that arise from the cellular organization into fibers and laminar sheets. Global conductivity values are obtained by combining ventricular fiber and sheet organization with myocyte-specific local conductivity values [51]. Current flow in the tissue is driven by active processes of ionic exchange across myocyte membranes (See also Chaps. 3 and 4). These active electrical processes are represented by the ionic model of myocyte membrane behavior, where current flow through ion channels, pumps, and exchangers in the myocyte membrane as well as subcellular Ca cycling between cell compartments and buffers are governed by a set of ordinary differential (ODE) and algebraic equations. Simultaneous solution of the PDE with the set of ionic model equations represents the simulation of electrical wave propagation in the heart. Our laboratory has extensive expertise in simulating electrical activity in the heart using this approach [4, 38, 45], where a biophysical model of myocyte active behavior is combined with a model of cardiac structure and geometry; review of all the modeling details can be found in [31].

9.6 Modeling of Electromechanics: General Aspects

To simulate cardiac electromechanics, the electrical component of the model (described in the previous section) is coupled to a mechanical component. A schematic of the electromechanical model is shown in Fig. 9.4. Physiologically, when an electrical wave propagates through the heart, the depolarization of each myocyte initiates a release of Ca from its intracellular Ca stores, followed by binding of Ca to Troponin C and cross-bridge cycling. The latter forms the basis for contractile protein movement and development of active tension in the cell, ultimately resulting in the deformation of the ventricles. Thus, the intracellular Ca released during the electrical activation couples the electrical and mechanical components. It serves as an input to a biophysical cell myofilament model representing the generation of

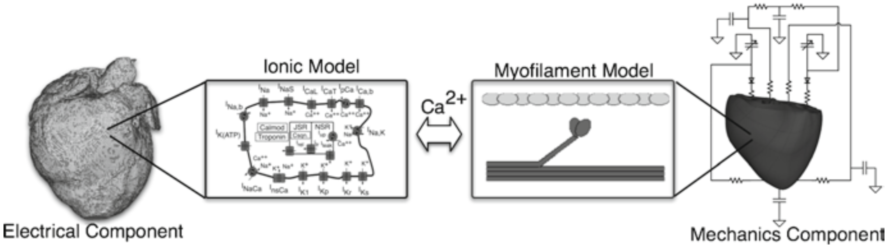

Fig. 9.4 Overall scheme of the image-based electromechanical model

active tension within each myocyte, where a set of ODEs and algebraic equations describe Ca binding to Troponin C, cooperativity between regulatory proteins, and cross-bride cycling.

Contraction of the ventricles arises from the active tension generated by the cardiac cells. Ventricular deformation is described by the equations of passive cardiac mechanics [17, 46, 47], with the myocardium being an orthotropic (due to fiber and laminar sheet organization), hyperelastic, and nearly incompressible material with passive mechanical properties defined by an exponential strain energy function. Simultaneous solution of the myofilament model equations with those representing passive cardiac mechanics on the finite element mechanical mesh constitutes the simulation of cardiac contraction. During contraction, the stretch ratio (i.e., the ratio of myocyte length before and after deformation) and its time derivative affect myofilament dynamics, including length-dependent Ca sensitivity, providing a feedback loop.

Finally, to simulate the cardiac cycle, conditions on chamber volume and pressure are imposed by a lumped-parameter model of the systemic and pulmonic circulatory systems, as shown in Fig. 9.4. The lumped-parameter model is based on the implementation by Kerckhoffs et al. [23], which we modified.

9.7 Cardiac Electrophysiology Modeling Example: Ventricular Tachycardia in the Infarcted Canine Heart

This section presents an example of the image-based electrophysiological model approach described above. It examines ventricular tachycardia (VT) in an image-based 3D model that incorporates accurate infarct geometry and composition. Complex myocardial remodeling that occurs in postinfarcted hearts has been shown to give rise to substrates that could initiate or anchor VT reentrant activity. The degree of myocardial injury in the infarcted region is dependent on tissue proximity from the site of occlusion. Tissue that experiences zero perfusion undergoes cellular necrosis and formation of scar tissue. Infarct-shape analysis has demonstrated that strands of viable tissue within electrically passive scar tissue could provide alternate pathways for propagation. In addition, partial perfusion in the adjacent peri-infarct zone tissue results in ion channel and gap junction remodeling that have been shown to result in slowed conduction and altered action potential morphology. The complexity of tissue remodeling within the infarct has made it difficult to elucidate the specific mechanisms that give rise to postinfarction VT and its morphology.

The model was built using previously described methods from an infarcted canine heart, which was scanned 4-week postinfarction using structural MR and DTMR at a resolution of $350 \times 350 \times 800\ \mu m^3$ and interpolated using cubic splines to a resolution of $200 \times 200 \times 200\ \mu m^3$. The top row in Fig. 9.5 shows the geometry of the model. The ionic kinetics in the normal myocardium and peri-infarct zone were represented by the Luo–Rudy dynamic model [26]. Membrane kinetics in the peri-infarct zone was modified based on data from literature. Previous studies of

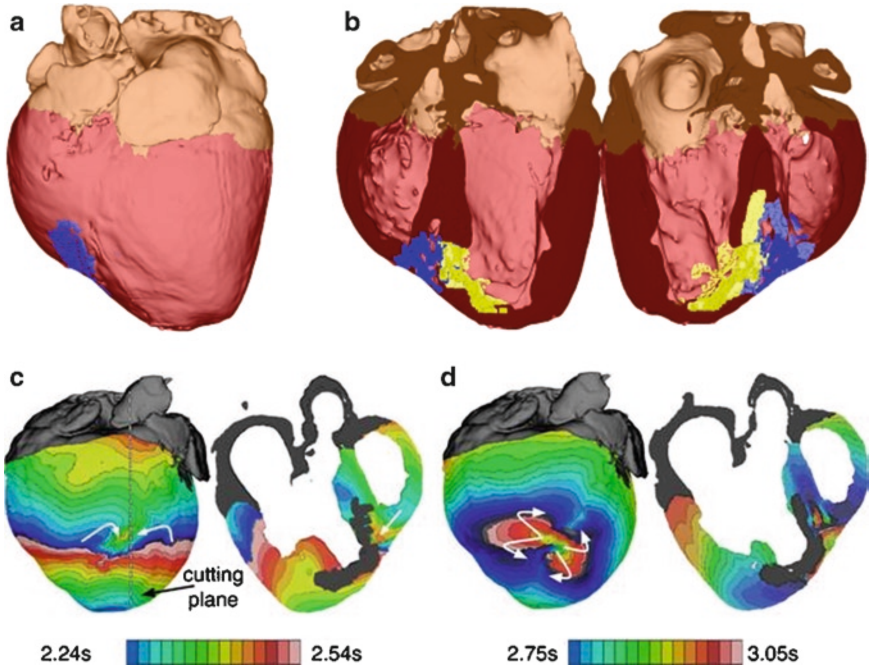

Fig. 9.5 The geometry of the infarcted canine heart model and activation times during VT induction. (**a**) Anterior view of geometry, where the ventricles are colored in *red*, atria in *chocolate brown*, infarct core in *yellow*, and peri-infarct zone in *blue*; (**b**) the geometry split in half along a horizontal view axis plane; (**c**) epicardial and transmural activation times during the fourth pacing stimulus; (**d**) activation map showing the VT circuit

peri-infarct zone in infarcted canine hearts have reported a reduction in peak sodium current to 38% of the normal value [35], in peak L-type calcium current to 31% of normal [13], and in peak potassium currents I_{Kr} and I_{Ks} to 30 and 20% of the maximum [22], respectively. These modifications result in longer action potential duration (APD) and decreased excitability compared to the normal myocardium. To examine the arrhythmogenic propensity of the infarct substrate, an aggressive pacing protocol was delivered from the apex, similar to protocols used for clinical evaluation of patients with myocardial infarction. Pacing commenced at a basic cycle length of 250 ms for five beats (S1); 450 ms after the last S1, six stimuli were delivered at progressively shorter coupling intervals, starting at 190 ms and decreasing in steps of 10 ms. The induced activity was monitored for additional 2.5 s.

The bottom row in Fig. 9.5 illustrates the events that lead to VT induction. It depicts isochrones of activation times for time periods during the fourth stimulus of the aggressive pacing protocol (panel c) and during the resulting VT (panel d). For each activation map, the image on the right presents the intramural activation pattern on a slice through the heart, the location of which is indicated by the white dotted line on the epicardium in panel c. When the propagating wavefront from the pacing site reaches the peri-infarct zone, conduction significantly slows as compared to the surrounding normal tissue. Faster wavefronts from the normal myocardium converge into the peri-infarct zone laterally (white arrows) activating the entire peri-infarct zone. The transmural view show late activation of the peri-infarct zone due to the wavefront propagating from the normal myocardium. Since the peri-infarct zone has a longer APD, it remains refractory, while the surrounding myocardium is fully recovered. As the pacing rate is increased, the wavefront encounters refractory tissue, resulting in conduction block. This region of block later becomes the conduit for wavefront propagation from the intramural PZ toward the surface. When pacing is completed, the activation from within the peri-infarct tissue develops into an epicardial quatrefoil reentry. The reentry core remains within the peri-infarct and is sustained throughout the simulation with a rotation frequency of 5 Hz.

Previous experimental studies of infarcted canine hearts have reported the induction of VT with epicardial reentry morphology [5]. The simulations revealed that decreased excitability, longer APD, and reduced conduction velocity throughout the peri-infarct zone promoted conduction block and wave break that develops into epicardial reentry. Furthermore, the simulation showed that the site of wave break and reentry formation occurred in both the epicardial and intramural portions of the peri-infarct zone. Thus, this study showcased the utility of image-based computational modeling in predicting sites of reentry formation and maintenance.

9.8 Cardiac Electromechanics Modeling Example: Electromechanical Delay in the Normal Canine Heart

Despite recent advancements in the understanding of the electromechanical activation sequence during normal sinus rhythm, characterization of the spatiotemporal interactions between electrical activation and mechanical contraction throughout the ventricular volume remains incomplete. This stems from the fact that current experimental techniques are limited by their inability to simultaneously evaluate the 3D electrical and mechanical activity of the heart at a high spatiotemporal resolution; therefore, alternative approaches must be undertaken. In this section, the image-based electromechanical model of the normal canine ventricles was employed to obtain insight into the 3D electromechanical activation sequence during the normal sinus rhythm. To do so, we examined the distribution of the electromechanical delay (EMD), the time interval between the onset of myocyte depolarization and that of myofiber shortening, throughout the ventricular volume during the normal sinus rhythm.

Sinus rhythm was simulated by stimulating the endocardial surface at specific locations as if activation originated from the Purkinje network. The timings and locations were adjusted until the activation pattern matched experimental data [14, 43]. We employed the canine ionic model in [16], in which we incorporated an

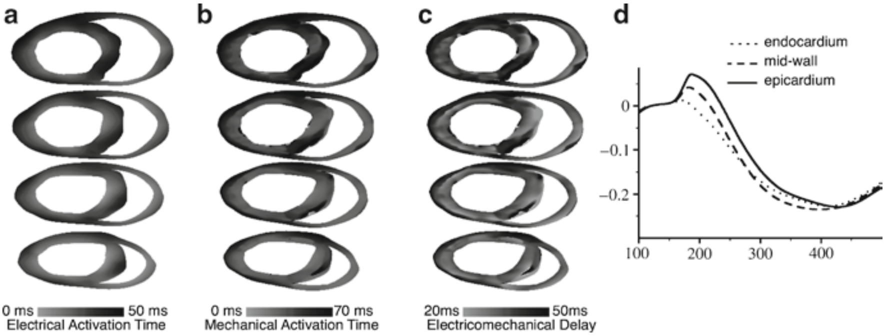

Fig. 9.6 Transmural, short-axis maps of electrical activation (**a**), mechanical activation (**b**), and electromechanical delay (**c**) during sinus rhythm in the normal canine heart. (**d**) Temporal traces of myofiber strain at the LV anterior wall

equation to represent Ca buffering by Troponin C [42]. Myofilament dynamics were governed by the biophysical model [36].

To determine the 3D distribution of EMD, the local time difference between myocyte depolarization and onset of myofiber shortening was calculated throughout the ventricles. Myocyte depolarization is defined as the instant at which the transmembrane potential exceeds 0 mV. Onset of shortening was defined as the instant when local myofiber shortening reaches 10% of its maximal value [41].

Transmural, short-axis maps of the electrical and mechanical activation (i.e., onset of myofiber shortening) times are shown in Fig. 9.6a and b, respectively. Electrical activation generally began from the endocardium and propagated to the epicardium and from the apex to the base; mechanical activation also followed this pattern. Transmural maps of EMD at the same short-axis views are shown in Fig. 9.6c and reveal that there are transmural differences in EMD throughout the LV free wall. EMD at the late-activated epicardium was longer than that at the early activated endocardium. To understand how these transmural differences in EMD arise, temporal traces of transmural myofiber strain at the mid-base of the anterior left ventricle are presented in Fig. 9.6d, and they demonstrate that the late-activated epicardium is prestretched, as indicated by the positive myofiber strain. This prestretch delays the onset of myofiber shortening and results in a prolonged EMD.

Previous experimental studies have shown that during normal sinus rhythm, there are differences in EMD on the epicardium between the apex and base [34, 41]. In addition, a local transmural difference in EMD has been reported at one single location at the anterior wall [6]. Our simulation results further these experimental findings and demonstrate that the 3D distribution of EMD is heterogeneous throughout the ventricular volume in the normal canine heart.

Understanding how this 3D distribution of EMD is altered under diseased conditions, such as dyssynchronous heart failure, and under different loading conditions could be particularly important to improving pacing therapies that aim to recoordinate mechanical contraction, such cardiac resynchronization therapy (CRT). Although CRT has been shown to improve quality of life and reduce hospitalizations [7], a substantial number of patients do not respond to CRT, making it difficult to justify the expense of its broader application (Chap. 10). Thus, further advancements in optimizing CRT delivery and improving the selection criteria of potential CRT responders will necessitate mechanistic insights into the 3D interaction between electrical activation and mechanical activation under healthy and diseased conditions.

9.9 On the Road to Patient-Specific Modeling

In the preceding sections, we described the methodologies that we have developed to construct representative models of cardiac structure and to study electrophysiological and electromechanical phenomena of the heart by simulating with numerical models. In this section, we present the techniques that we have developed to build models that are based on the specific architecture and electromechanical properties of the patient's diseased heart. Such personalized cardiac models in combination with high-performance computing can provide clinical researchers with quick and noninvasive access to critical information about electrophysiological and electromechanical phenomena and events in the hearts of individual patients. Ultimately, such patient-specific information will aid physicians to arrive at highly personalized decisions for electrophysiological interventions as well as prophylaxis, thereby dramatically improving cardiac healthcare. To illustrate, current radiofrequency ablation approaches to treating ventricular arrhythmia rely solely on the physician's experience in identifying and destroying the arrhythmogenic substrate, a task that is complicated by the variations in the morphology of structural remodeling (infarct) across different patients (Chap. 1). With the aid of realistic patient-specific computational models, physicians will be able to simulate different ablation scenarios, predict the results, and select the optimal intervention.

Despite the potential impact, the application of electrophysiological simulations in personalized treatment is hampered by a significant barrier, namely the lack of technology to acquire the fiber structure of a given patient heart. While advanced MR and CT technologies can acquire the geometry of a patient heart in vivo up to submillimeter resolution [15, 28, 30], there is no practical method that physicians can use for noninvasively acquiring the fiber structure of a living patient heart. This limitation constitutes one of the major obstacles to the application of computational cardiac simulations in the clinical setting. To address this need, we have developed a methodology to predict fiber orientations of a patient heart from geometry acquired in vivo [50].

We hypothesize that fiber orientations of a patient heart can be accurately predicted given the geometry of the patient heart and an atlas human heart. If this hypothesis was proven, it will be possible to estimate fiber orientations of patient hearts from geometries acquired using modern in vivo MRI and CT technologies. We have tested this hypothesis, and developed, using state-of-the-art techniques, a processing pipeline for the estimation of patient-specific fiber orientations. The pipeline involves the use of tools of computational anatomy [9] to morph fiber

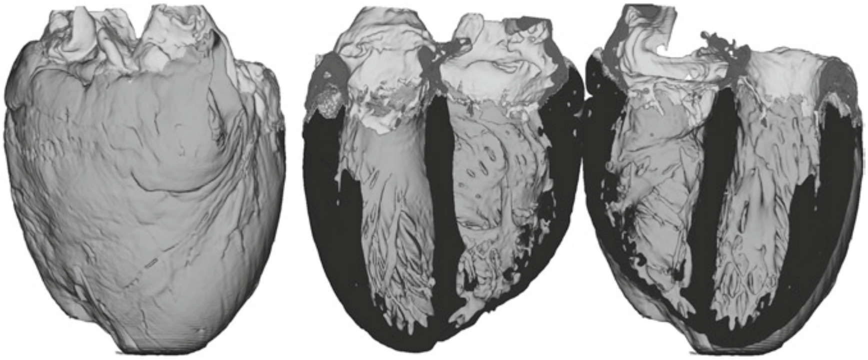

Fig. 9.7 The geometry of the normal human atlas heart. The *left panel* shows the anterior view, and the *right panel* shows the atlas split in half along a horizontal view axis plane. The ventricles appear in *dark gray*, and the atria in *light gray*

orientations of an atlas to match patient geometries (see, e.g., Chap. 7), thereby obtaining patient-specific fiber orientations.

The atlas is a normal human heart whose geometry and fiber orientations are acquired ex vivo using high-resolution ($0.4297 \times 0.4297 \times 1$ mm^3) structural MRI and DTMR image, respectively. The reconstruction of the atlas geometry from the structural data was performed using methods described in the previous section on image segmentation. Figure 9.7 shows the atlas geometry. The reconstruction is highly detailed, retaining finer structures such as trabeculations and papillary muscles. A visualization of the atlas fiber orientations is shown in Fig. 9.8. As expected, the fibers form a counterclockwise helix on the epicardial surface.

9.9.1 Processing Pipeline for Estimating Patient-Specific Fiber Orientations

Figure 9.9a shows the processing pipeline that we have developed to estimate patient-specific fiber orientations of the heart. The pipeline involves three main steps, as shown in the gray blocks in the figure. The following subsections describe these steps and illustrate our methodology by showing how the estimation is performed for an example patient who was scanned using in vivo CT.

9.9.2 Reconstruction of Patient Heart Geometry

In the first step, the patient heart structural MR or CT image is segmented to reconstruct the ventricular myocardium. In this segmentation, the voxels that correspond to the ventricular myocardium of the patient heart are labeled. The labeling is performed

Fig. 9.8 A visualization of the fiber orientations in the normal human heart atlas

by fitting closed splines through a set of landmark points that are semiautomatically placed along the epicardial and endocardial boundaries of the ventricles in the image. All voxels that lie inside the epicardial spline, but outside the endocardial splines are marked as myocardial. Similar to the extraction of ventricles from a high-resolution ex vivo image described previously, the placement of landmark points is performed manually for a number of slices that are evenly distributed in the image. The landmark points for the remaining slices are obtained automatically by linearly interpolating the manually identified points. Figures 9.9b and c illustrate the reconstruction of the ventricular geometry from the in vivo CT image of the example patient. Incidentally, our experiments indicate that the number of image slices for which landmark points need to be placed manually is about 10% of the total number of slices, and the amount of time required for segmenting the myocardium from a typical in vivo image is less than 1 h.

9.9.3 Deformation of Atlas Heart Geometry

In the next step of the pipeline, the ventricular myocardium of the atlas heart is deformed to match the patient heart geometry. This deformation is performed in two phases. The first phase involves an affine transformation based on a set of landmarks points. Five manually identified landmarks, including the LV apex, the right ventriculoseptal junctions located at the base, and the right ventriculoseptal

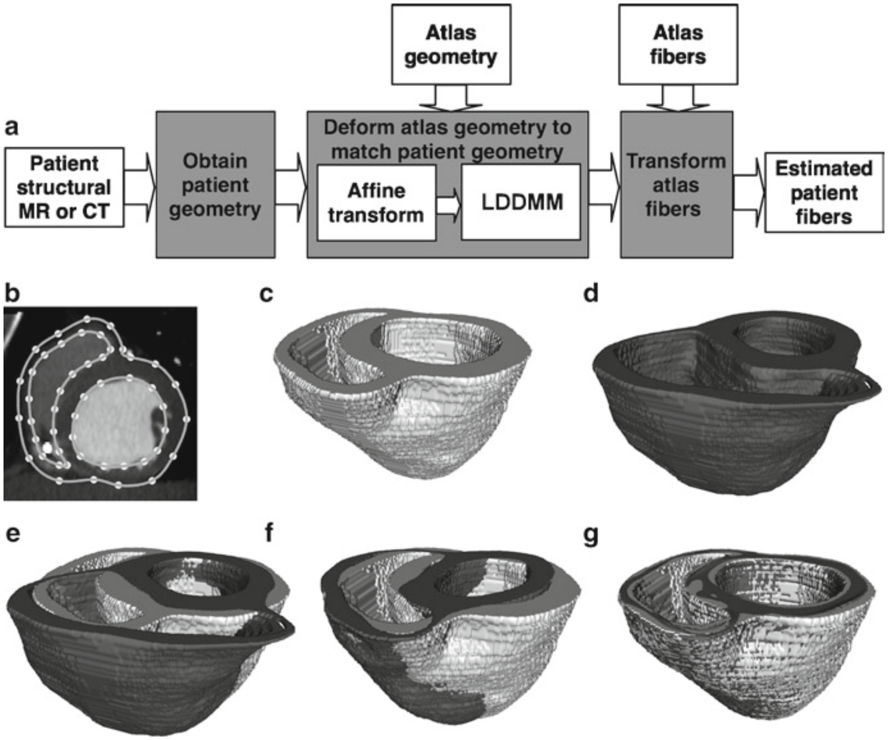

Fig. 9.9 Our methodology for estimating patient-specific myocardial fiber orientations. (**a**) The processing pipeline for the estimation; (**b**) segmentation of an example patient heart image, where splines are shown in *gray* and landmarks in *white*; (**c**) ventricular geometry of the example patient heart; (**d**) the ventricular myocardium of the atlas; (**e**) patient and atlas ventricular geometries superimposed; (**f**) patient geometry and affine transformed atlas geometry; (**g**) patient geometry and atlas geometry after large deformation diffeomorphic metric mapping (LDDMM)

junctions located midway between base and apex are used. Figure 9.9d shows the ventricular myocardium of the atlas heart, which is shown in Fig. 9.7. Figure 9.9e shows the patient geometry from Fig. 9.9c, together with the atlas ventricular myocardium. Figure 9.9f shows the patient geometry and the affine transformed atlas geometry.

The second phase of deformation of atlas geometry involves a high-dimensional nonlinear deformation using an algorithm known as large deformation diffeomorphic metric mapping (LDDMM) [10]. The advantage of the LDDMM algorithm is two-fold. First, it computes transformations that are smooth and invertible (diffeomorphic), thereby preserving the integrity of anatomical structures during deformation. In particular, connected sets remain connected and disjoint sets remain disjoint, smoothness of anatomical structures such as curves and surfaces is preserved, and coordinates are transformed consistently. Secondly the algorithm computes a geodesic, which is the shortest length path in the space of transformations that match the template and target, thereby quantifying the deformation via a scalar metric distance, and providing a superior registration quality. The deformation of the atlas geometry, using the affine transformation and LDDMM, matches the atlas geometry with the patient geometry. Figure 9.9g shows the patient geometry together with the atlas geometry after LDDMM deformation. The deformed atlas closely matches the patient geometry.

9.9.4 Deformation of Atlas Fiber Orientations

In the final step of the pipeline, the fiber orientations of the patient heart are estimated. This step involves the application of the affine transformation matrix and the deformation field of LDDMM in sequence to deform the DTMR image of the atlas. The deformation of the DTMR image consists of spatial repositioning of the image voxels in accordance with the spatial transformation of geometry images and reorientation of the DTs. The reorientation of the DTs is performed by using the so-called preservation of principal directions method [2]. This method preserves the principal direction of the DT as well as the plane spanned by the largest two eigenvectors, and therefore is well suited for the higher-order transformations that are involved in registering cardiac images. The deformation of the template DTMR image, by repositioning the image voxels and reorienting the DTs, gives an estimate of the patient heart DTs, the primary eigenvectors of which provide an estimate of the patient-specific fiber orientations. Figure 9.10 shows the estimated myocardial fiber orientations of the example patient. As expected, the fiber orientations appear clockwise helically near the endocardium, circumferentially near midwall, and anticlockwise helically near the epicardium.

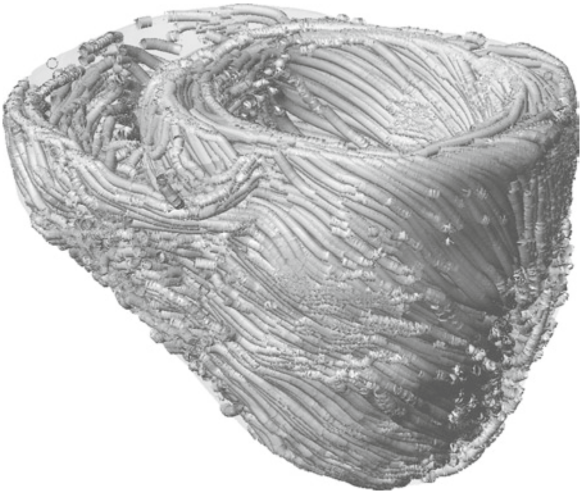

Fig. 9.10 A visualization of the estimated myocardial fiber orientations of the example patient

9.9.5 Pipeline Validation

The pipeline for estimating patient-specific fiber orientations was validated using six normal, one failing, and one infarcted canine hearts, all of which were scanned ex vivo with high-resolution DTMR to obtain ground truth fiber orientations. One normal canine heart was chosen as the "atlas" and the fiber orientations of all other hearts were estimated. The error in estimated fiber orientations was computed as the absolute difference between the inclination angles [40] of estimated orientations and ground truth orientations. It was found that the mean error in the normal, failing, and infarcted cases were 14, 14.3, and 18°, respectively. The overall mean error was 14.8°, which is comparable to the error of 12° in fiber orientations derived from DTMR images [40].

In addition to the above, we conducted simulations of paced propagation with ventricular models built using estimated and ground truth fiber orientations and compared the resulting activation time values. In normal canine hearts, simulations showed a difference of 7.8% in activation timing values between models built using ground truth fiber orientations and those using estimated fiber orientations. In failing and infarcted cases, the differences were 7.7 and 6.2%, respectively. These results show that the estimated fiber orientations can be reliably used in electrophysiological simulations.

9.10 Conclusion

In conclusion, we have developed methods to construct high-resolution representative models of the whole-heart electrophysiology and electromechanics from images acquired ex vivo. Simulations with these models can provide new insights into cardiac function, in health and disease. Building upon our research in constructing representative models of the heart, we have developed a pipeline to create patient-specific computational meshes of the heart from in vivo images. The pipeline involves a method to accurately predict fiber orientations of patient hearts and constitutes a step toward patient-specific models of cardiac electrophysiology.

References

1. Adams, R. and L. Bischof (1994). "Seeded Region Growing." IEEE Transactions on Pattern Analysis and Machine Intelligence **16**(6): 641–647.
2. Alexander, D. C., C. Pierpaoli, et al. (2001). "Spatial Transformations of Diffusion Tensor Magnetic Resonance Images." IEEE Transactions on Medical Imaging **20**(11): 1131–1139.
3. Arsigny, V., P. Fillard, et al. (2006). "Log-Euclidean Metrics for Fast and Simple Calculus on Diffusion Tensors." Magnetic Resonance in Medicine **56**: 411–421.
4. Ashihara, T., J. Constantino, et al. (2008). "Tunnel Propagation of Postshock Activations as a Hypothesis for Fibrillation Induction and Isoelectric Window." Circulation Research **102**(6): 737–745.

5. Ashikaga, H., T. Sasano, et al. (2007). “Magnetic Resonance-Based Anatomical Analysis of Scar-Related Ventricular Tachycardia: Implications for Catheter Ablation.” Circulation Research **101**: 939–947.
6. Ashikaga, H., B. A. Coppola, et al. (2008). “Transmural Dispersion of Myofiber Mechanics: Implications for Electrical Heterogeneity In Vivo.” Journal of American College of Cardiology **49**(8): 909–916.
7. Auricchio, A., C. Stellbrink, et al. (2003). “Clinical Efficacy of Cardiac Resynchronization Therapy Using Left Ventricular Pacing In Heart Failure Patients Stratified By Severity of Ventricular Conduction Delay.” Journal of American College of Cardiology **42**(12): 2109–2116.
8. Basser, P. J. and C. Pierpaoli (1996). “Microstructural and Physiological Features of Tissues Elucidated by Quantitative-Diffusion-Tensor MRI.” Journal of Magnetic Resonance **111**(3): 209–219.
9. Beg, M. F., P. A. Helm, et al. (2004). “Computational Cardiac Anatomy Using MRI.” Magnetic Resonance in Medicine **52**(5): 1167–1174.
10. Beg, M. F., M. I. Miller, et al. (2005). “Computing Large Deformtion Metric Mppings via Geodesic Flows of Diffeomorphisms.” International Journal of Computer Vision **61**(2): 139–157.
11. Burton, R. A. B., G. Plank, et al. (2006). “Three-Dimensional Models of Individual Cardiac Histoanatomy: Tools and Challenges.” Annals of the New York Academy of Sciences **1080**: 301–319.
12. Chen, J., S.-K. Song, et al. (2003). “Remodeling of Cardiac Fiber Structure After Infarction In Rats Quantified With Diffusion Tensor MRI.” American Journal of Physiology. Heart and Circulatory Physiology **285**(3): H946–H954.
13. Dun, W., S. Baba, et al. (2004). “Dynamic Remodeling of K^+ and Ca^{2+} Currents in Cells that Survived in the Epicardial Border Zone of Canine Healed Infarcted Heart.” American Journal of Physiology. Heart and Circulatory Physiology **287:** 1046–1045.
14. Durrer, D., R. T. v. Dam, et al. (1970). “Total Excitation of the Isolated Human Heart.” Circulation **41**(6): 899–912.
15. Fayad, Z. A., V. Fuster, et al. (2002). “Computed Tomography and Magnetic Resonance Imaging for Noninvasive Coronary Angiography and Plaque Imaging.” Circulation **106**: 2026–2034.
16. Fox, J. J., J. L. McHarg, et al. (2002). “Ionic Mechanism of Electrical Alternans.” American Journal of Physiology. Heart and Circulatory Physiology **282**(2): H516–H530.
17. Guccione, J. M., K. D. Costa, et al. (1995). “Finite Element Stress Analysis of Left Ventricular Mechanics in the Beating Dog Heart.” Journal of Biomechanics **28**(10): 1167–1177.
18. Helm, P., M. F. Beg, et al. (2005). “Measuring and Mapping Cardiac Fiber and Laminar Architecture Using Diffusion Tensor MR Imaging.” Annals of the New York Academy of Sciences **1047**: 296–307.
19. Helm, P. A., H.-J. Tseng, et al. (2005). “Ex Vivo 3D Diffusion Tensor Imaging and Quantification of Cardiac Laminar Structure.” Magnetic Resonance in Imaging **54**(4): 850–859.
20. Helm, P. A., L. Younes, et al. (2006). “Evidence of Structural Remodeling in the Dyssynchronous Failing Heart.” Circulation Research **98**(1): 125–132.
21. Ibanez, L., W. Schroeder, et al. (2003). The ITK Software Guide: The Insight Segmentation and Registration Toolkit, Albany, NY, Kitware Inc.
22. Jiang, M., C. Cabo, et al. (2000). “Delayed Rectifier K Currents Have Reduced Amplitudes and Altered Kinetics in Myocytes from Infarcted Canine Ventricle.” Cardiovascular Research **48**: 34–43.
23. Kerckhoffs, R. C., M. L. Neal, et al. (2007). “Coupling of a 3D Finite Element Model of Cardiac Ventricular Mechanics to Lumped Systems Models of the Systemic and Pulmonic Circulation.” Annals of Biomedical Engineering **35**(1): 1–18.
24. Law, M. W. K. and A. C. S. Chung (2007). “Weighted Local Variance-Based Edge Detection and Its Application to Vascular Segmentation in Magnetic Resonance Angiography.” IEEE Transactions on Medical Imaging **26**(9): 1224–1241.
25. Lesko, L. J. (2007). “Personalized Medicine: Elusive Dream or Imminent Reality.” Clinical Pharmacology and Therapeutics **81**(6): 807–816.

26. Luo, C. and Y. Rudy (1994). “A Dynamic Model of the Cardiac Ventricular Action Potential. I. Simulations of Ionic Currents and Concentration Changes.” Circulation Research **74**: 1071–1096.
27. Nielsen, P. M. F., I. J. Legrice, et al. (1991). “Mathematical Model of Geometry and Fibrous Structure of the Heart.” American Journal of Physiology. Heart and Circulatory Physiology **260**(4): H1365–H1378.
28. Nikolaou, K., T. Flohr, et al. (2004). “Advances in Cardiac CT Imaging: 64-Slice Scanner.” International Journal of Cardiovascular Imaging **20**(6): 535–540.
29. Noble, D. (2002). “Modeling the Heart – From Genes to Cells to the Whole Organ.” Science **295**(5560): 1678–1682.
30. Peters, D. C., D. B. Ennis, et al. (2002). “High-Resolution MRI of Cardiac Function with Projection Reconstruction and Steady-State Free Precession.” Magnetic Resonance in Medicine **48**(1): 82–88.
31. Plank, G., L. Zhou, et al. (2008). “From Mitochondrial Ion Channels to Arrhythmias in the Heart: Computational Techniques to Bridge the Spatio-Temporal Scales.” Philosophical Transactions Series A, Mathematical, Physical, and Engineering Sciences **366**(1879): 3381–3409.
32. Plank, G., R. A. B. Burton, et al. (2009). “Generation of Histo-anatomically Representative Models of the Individual Heart: Tools and Application.” Philosophical Transactions of the Royal Society A **367**(1896): 2257–2292.
33. Prassl, A. J., F. Kickinger, et al. (2009). “Automatically Generated, Anatomically Accurate Meshes for Cardiac Electrophysiology Problems.” IEEE Transactions on Biomedical Engineering **56**(5): 1318–1330.
34. Prinzen, F. W., C. H. Augustijn, et al. (1992). “The Time Sequence of Electrical and Mechanical Activation During Spontaneous Beating and Ectopic Stimulation.” European Heart Journal **13**(4): 535–543.
35. Pu, J. and P. A. Boyden (1997). “Alterations of Na+ Currents in Myocytes from Epicardial Border Zone of the Infarcted Heart A Possible Ionic Mechanism for Reduced Excitability and Postrepolarization Refractoriness.” Circulation Research **81**: 110–119.
36. Rice, J. J., F. Wang, et al. (2008). “Approximate Model of Cooperative Activation and Crossbridge Cycling in Cardiac Muscle Using Ordinary Differential Equations.” Biophysical Journal **95**(5): 2368–2390.
37. Rodgers, A. and P. Vaughan (2002). The World Health Report 2002. Geneva, Switzerland, The World Health Organization.
38. Rodríguez, B., J. C. Eason, et al. (2006). “Differences Between Left and Right Ventricular Anatomy Determine the Types of Reentrant Circuits Induced by an External Electric Shock. A Rabbit Heart Simulation Study.” Progress in Biophysics and Molecular Biology **90**(1–3): 399–413.
39. Schmidt, A., C. F. Azevedo, et al. (2007). “Infarct Tissue Heterogeneity by Magnetic Resonance Imaging Identifies Enhanced Cardiac Arrhythmia Susceptibility in Patients with Left Ventricular Dysfunction.” Circulation **115**(15): 2006–2014.
40. Scollan, D. F., A. Holmes, et al. (1998). “Histological Validation of Myocardial Microstructure Obtained from Diffusion Tensor Magnetic Resonance Imaging.” American Journal of Physiology. Heart and Circulatory Physiology **275**(6): H2308–H2318.
41. Sengupta, P. P., B. K. Khandheria, et al. (2006). “Apex-to-Base Dispersion in Regional Timing of Left Ventricular Shortening and Lengthening.” Journal of American College of Cardiology **47**(1): 163–172.
42. Solovyova, O., L. Katsnelsona, et al. (2002). “Mechanical Inhomogeneity of Myocardium Studied in Parallel and Serial Cardiac Muscle Duplexes: Experiments and Models.” Chaos, Solitons and Fractals **13**(8): 1685–1711.
43. Spach, M. S. and R. C. Barr (1975). “Ventricular Intramural and Epicardial Potential Distributions During Ventricular Activation and Repolarization in the Intact Dog.” Circulation Research **37**(2): 243–257.
44. Thrall, J. H. (2004). “Personalized Medicine.” Radiology **231**: 613–616.

45. Trayanova, N., F. Aguel, et al. (2004). Modeling Cardiac Defibrillation: An Inquiry into Post-shock Dynamics. Cardiac Electrophysiology: From Cell to Bedside, Philadelphia, Saunders, 282–291.
46. Usyk, T. P., R. Mazhari, et al. (2000). "Effect of Laminar Orthotropic Myofiber Architecture on Regional Stress and Strain in the Canine Left Ventricle." Journal of Elasticity **61**: 143–164.
47. Usyk, T. P., I. J. L. Grice, et al. (2002). "Computational Model of Three Dimensional Cardiac Electromechanics." Computing and Visualization in Science **4**(4): 249–257.
48. Vadakkumpadan, F., H. Arevalo, et al. (2008). "Image-Based Models of Cardiac Structure in Health and Disease." Wiley Interdisciplinary Reviews: Systems Biology and Medicine **2**(4): 489–506.
49. Vadakkumpadan, F., L. J. Rantner, et al. (2009). "Image-Based Models of Cardiac Structure with Applications in Arrhythmia and Defibrillation Studies." Journal of Electrocardiology 42(2): 157.e1–157.e10.
50. Vadakkumpadan, F., H. Arevalo, et al. (2009). "Image-Based Estimation of Myocardial Fiber Orientations for Patient-Specific Models of Cardiac Electrophysiology." Heart Rhythm **6**(11): 1688.
51. Vigmond, E., F. Vadakkumpadan, et al. (2009). "Towards Predictive Modelling of the Electrophysiology of the Heart." Experimental Physiology **94**(5): 563–577.
52. Whiteley, P. (2007). The Case for Personalized Medicine. 14th International Tri-Conference on Molecular Medicine, San Francisco, CA, Moscone convention center.
53. Wu, M.-T., W.-Y. I. Tseng, et al. (2006). "Diffusion Tensor Magnetic Resonance Imaging Mapping the Fiber Architecture Remodeling in Human Myocardium After Infarction: Correlation With Viability and Wall Motion." Circulation **114**(10): 1036–1045.